Title

Bridging knowledge gaps in liquid- and vapor-fed CO2 electrolysis through active electrode area

Journal

Chem Catalysis, 2(11)

ISSN

2667-1107

Authors

Corral, Daniel
Lee, Dong Un
Ehlinger, Victoria M
et al.

Publication Date

2022-11-01

DOI

10.1016/j.checat.2022.09.017

Bridging knowledge gaps in liquid- and vapor-fed CO_2 electrolysis using catalyst surface area

Daniel Corral†[1,2], Dong Un Lee†[1], Victoria M. Ehlinger[3], Stephanie Nitopi[1], Jaime E. Avilés Acosta[1], Lei Wang[1], Alex J. King[4], Jeremy T. Feaster[5], Yi-Rung Lin[1], Adam Z. Weber[4], Sarah E. Baker[5], Eric B. Duoss[2], Victor A. Beck[*3], Christopher Hahn[*5], and Thomas F. Jaramillo[*1,6]

† These authors contributed equally to this work

*Correspondence should be addressed to beck33@llnl.gov, hahn31@llnl.gov and jaramillo@stanford.edu

Affiliations:

1. SUNCAT Center for Interface Science and Catalysis, Department of Chemical Engineering, Stanford University, Stanford, CA 94305, USA. E-mail: jaramillo@stanford.edu

2. Materials Engineering Division, Lawrence Livermore National Laboratory, Livermore, CA 94550, USA.

3. Computational Engineering Division, Lawrence Livermore National Laboratory, Livermore, CA 94550, USA. E-mail: beck33@llnl.gov

4. Energy Conversion Group and Liquid-Sunlight Alliance, Lawrence Berkeley National Laboratory, Berkeley, CA 94720, USA.

5. Materials Science Division, Lawrence Livermore National Laboratory, Livermore, CA 94550, USA. E-mail: hahn31@llnl.gov

6. SUNCAT Center for Interface Science and Catalysis, SLAC National Accelerator Laboratory, Menlo Park, CA 94025, USA.

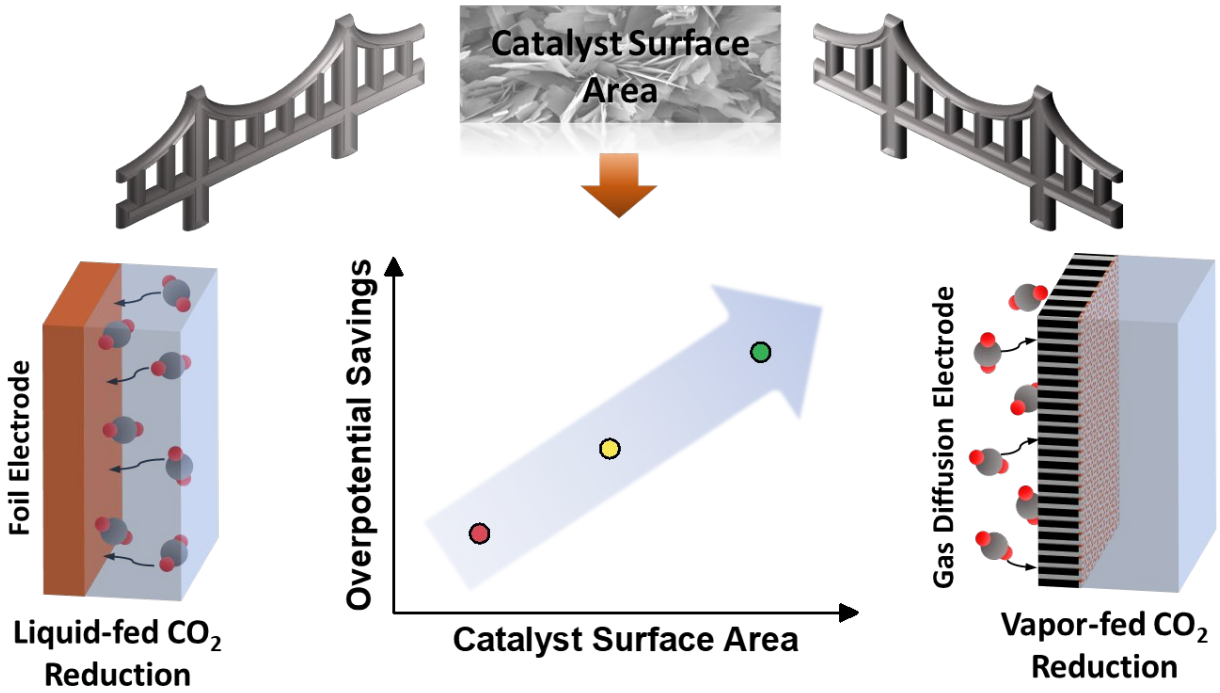

TOC Figure

We achieve a ~700-fold and ~10-fold increase in multi-carbon product formation by designing roughened catalysts for both foil- and gas diffusion-type electrodes, respectively. We showcase catalyst surface area as a key descriptor for understanding the interplay between the electrode structure and local reaction environment on activity and selectivity. Both experimental and computational modeling determine heightened reaction rates towards CO_2R at lower overpotentials, which uncover a clear dependence on electrode roughness.

Highlights

- Distinct catalyst morphologies are translated between electrode types
- Reaction rate toward CO_2R and C_{2+} products is enhanced at lower overpotentials
- Increase in J_{geo} up to ~735x and ~10x are observed with foil and GDEs, respectively
- Experiments and model show Tafel-like description of roughness and potential shift

Summary

Increased use of gas-diffusion electrodes for CO_2 electroreduction widens the experimental phase space (i.e., increased reaction rate and mass transport) that was previously inaccessible using foil electrodes. This raises fundamental questions over the impacts of key variables that translate between liquid- and vapor-fed CO_2 electrolysis systems, warranting comparisons to aid our understanding of the underlying processes that control performance. In this work, we studied the interplay of current-potential profiles and electrode roughness on product activity and selectivity for both liquid- and vapor-fed CO_2 reduction. We implement a Cu nanoflower morphology on both electrode architectures, allowing us to tune the electrochemically active surface area (ECSA) and thus overpotential. This results in decreased overpotentials as high as 460 and 174 mV for foil and gas diffusion electrodes, respectively, while maintaining or improving multi-carbon product current density. We further investigate these overpotential shifts and product activities by normalizing the current density by ECSA, uncovering current-potential relationships akin to those of the Tafel description. A continuum, 1D steady-state model rationalized the shifts, demonstrating that Tafel-like kinetics are useful for describing the roughness dependence for both liquid- and vapor-fed systems. This analysis establishes a holistic approach for establishing key catalyst design criterion that guide the development of improved materials and devices for CO_2 electrolysis technologies.

The bigger picture

CO_2 electrolysis is an attractive method for producing industrially relevant chemicals while reducing emissions coupled with renewable energy sources. Recent advancements have focused on evolving the electrode architecture from metal foils to porous gas diffusion electrodes for improving the reaction rate. However, the contributions from surface kinetics and local reaction environment are convoluted and vary when translating from liquid- to vapor-fed systems. Herein, we draw connections between these systems by evaluating identical catalyst structures of varying roughness for both electrode types. Our experimental and modeling approaches provide better understanding of the interplay between electrode structure and reaction environment on the activity and selectivity. We observe nominal changes in the intrinsic activity of Cu with significant overpotential savings corresponding to the roughness factors across electrode types.

1. Introduction

Increased accessibility and rapidly declining costs of renewable technologies have incentivized gradual decarbonization in the global energy landscape.[1,2] However, other energy services essential to modern civilization cause emissions that will be more difficult to eliminate fully, such as aviation, long-distance transportation and shipping, and production of carbon intensive structural materials.[3] To address these and other remaining emissions, methods of carbon capture and sequestration are being developed to remove CO_2 from air and point sources of emissions, requiring further development and cooperative policy for economic viability.[4,5] Thus, there is great motivation to utilize CO_2 after it has been captured to make valuable products.[6] Electrochemical CO_2 reduction (CO_2R) has risen as a promising candidate in that regard based on two criteria, including: (1) the ability to address emissions while producing essential carbon-based fuels and chemicals,[7] and (2) CO_2R can be coupled with intermittent renewable technologies such as wind and solar power, to convert electricity to more versatile forms of chemical energy for storage and transportation.[8]

Knowledge gained from liquid-fed systems has provided a strong foundation for vapor-fed devices using gas-diffusion electrodes (GDEs) as the field focuses on industrial implementation. For both systems – which use aqueous electrolytes – complicated surface kinetics and competing homogeneous and hydrogen-evolution reactions (HER) limit performance.[9–11] More recently, the concept of the microenvironment (i.e. local reaction environment) in cooperation with polarization and surface effects has helped frame our understanding of device performance.[12] For foil electrodes in liquid-fed devices, roughening likely does not increase the intrinsic activity of Cu towards CO_2R;[9,13] yet, it does influence product selectivity due to nano- and meso-scale effects.[14–17] Differences in selectivity have been attributed to varying coordination number,[18–23] pore size and shape,[24,25] and subsurface oxygen.[26] Ren et al. demonstrated changing selectivity based on the potential window[27] and De Luna et al. have correlated C_2H_4 activity with suppressed CH_4 formation,[28] both achieved via nanostructuring. This also changes the local pH[14,15,29], which can suppress the HER rate and promote C_{2+} selectivity.[28,30–32] Naturally, the strategy for operating at low overpotential in

alkaline electrolytes has resulted in nearly full selectivity towards multi-carbon products from CO reduction.[33] By extension, these criteria have been employed for enhanced CO_2R performance in vapor-fed systems; GDEs permit highly active CO_2R in alkaline electrolytes (e.g. KOH) while minimizing species diffusion lengths in thin catalyst layers.[31,34] Such systems have been able to target multi-carbon production at lower overpotentials by controlling the microenvironment; which there are likely many more when using GDEs compared to foil electrodes.[12,31,34–36] Yet, it is unclear what effects translate between environments by nanostructuring the catalyst layer.

In this work, we utilize catalyst surface area to provide insight and bridge knowledge gaps between two different systems; liquid- and vapor-fed CO_2R electrolyzers that utilize foil electrodes and GDEs, respectively (Figure S1). We observe the complex interplay between overarching potential-dependent trends, microenvironment, and electrodes of varying design and roughness factor (RF). We propose that the CO_2R selectivity trends and catalyst design strategies for tuning product formation in liquid-fed CO_2 electrolysis extend to the vapor-fed systems (Figure 1). That is, (1) at a constant overpotential, the geometric current density will increase with increasing RF and (2) at constant geometric current density, the overpotential will decrease with increasing RF, both of which can affect product selectivity. By utilizing Cu nanoflower (NF) catalysts with intermediate RFs (e.g. ~185), we observe enhancements in multi-carbon (C_{2+}) production at lower overpotentials. Activity and selectivity trends are further explored by comparing the formation of products accounting for electrode RF. More importantly, the overpotential savings are proportional to the ratio of RFs between electrodes at similar geometric current densities, regardless of the electrode architecture. We corroborate and explain these findings via computational Multiphysics modeling of kinetics with local species transport to estimate differences in microenvironment. Tafel parameters derived from the foil electrodes are used to predict the current densities for GDEs of varying RF, showcasing RF dependence. In this way, a more generalized catalyst-design criterion is established; namely, the surface area should be targeted to specific current-potential regimes that enhance product selectivity or increase energy efficiency.

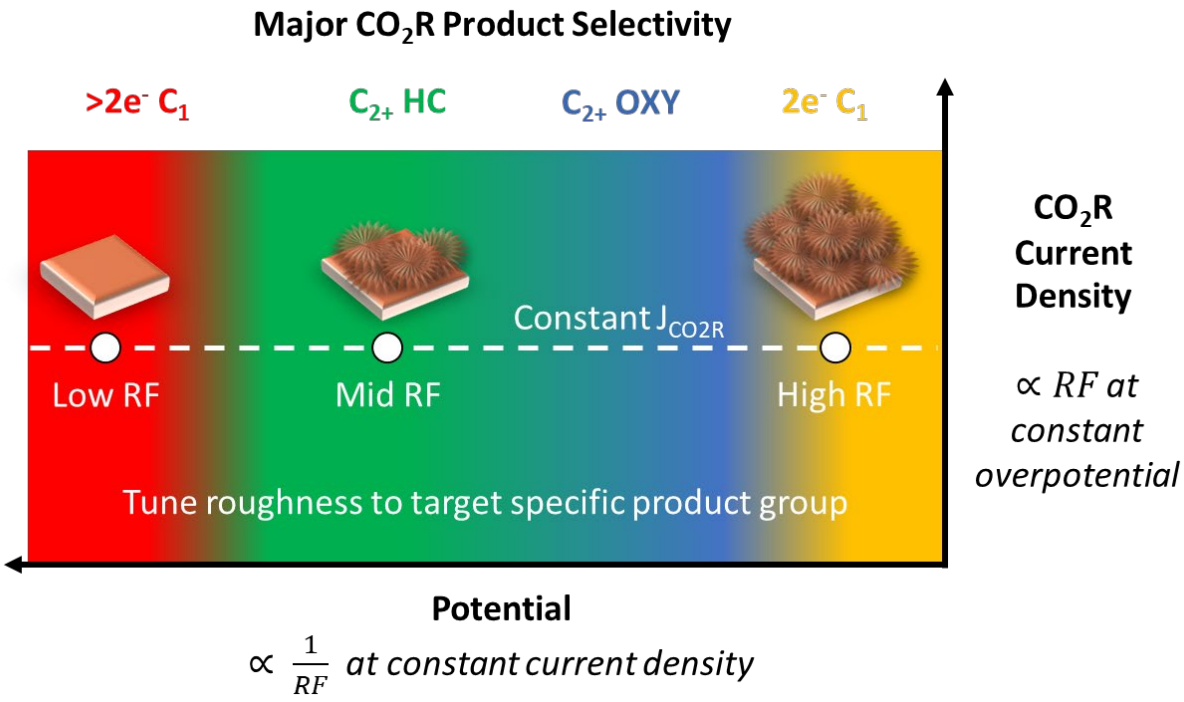

Figure 1. CO_2R electrode development strategy using RF

Effect of electrode roughness on geometric current density, electrochemical potential, and major CO_2R product selectivity for liquid- and vapor-fed CO_2 reduction. Product groups are defined as $2e^-$ single-carbon ($2e^-$ C_1), $>2e^-$ single-carbon ($>2e^-$ C_1), multi-carbon hydrocarbon (C_{2+} HC), and multi-carbon oxygenate (C_{2+} OXY). η and CO_2R Current Density represent overpotential and geometric current density, respectively. Relationships of potential and current density (x- and y-axes, respectively) with respect to RF are depicted.

2. Results and Discussions

2.1. Synthesis and characterization of electrode morphology

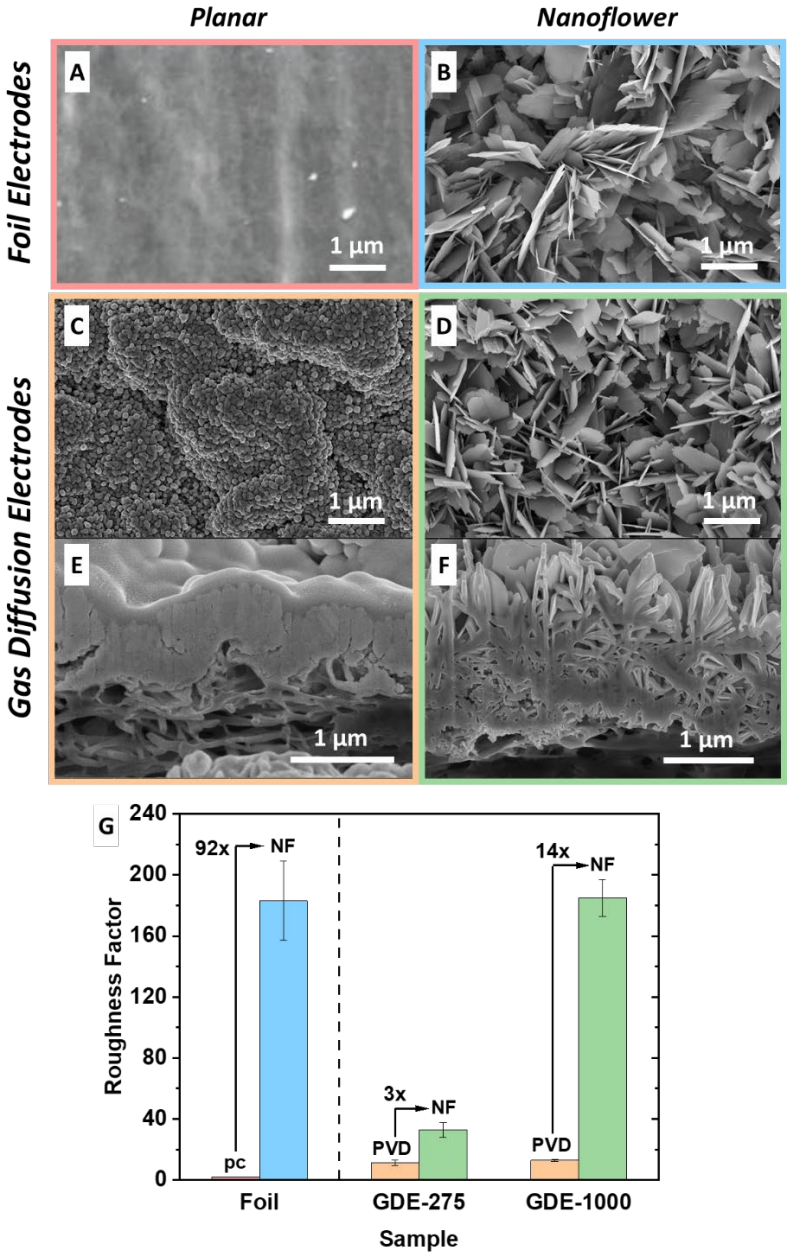

Figure 2. Nanoflower catalyst design and physical characterization

(A-D) top view SEM images of (A) foil polycrystalline copper, (B) foil nanoflower copper, (C) PVD GDE, and (D) nanoflower GDE.

(E and F) Cross-section view SEM images of (E) PVD GDE, and (F) nanoflower GDE.

(G) Roughness factor comparisons of foil and GDE samples before and after nanoflower formation.

To modulate the surface area of the active catalyst layer readily, we employed a facile etching technique based on a previously reported procedure,[33] where $(NH_4)_2S_2O_8$ oxidatively etches the surface of polycrystalline copper foil[37] (foil-pc) to form 3-dimensional self-assembled nanoflower structures (foil-NF) (Figure S2). The surface conversion from foil-pc (Figure 2A) to foil-NF (Figure 2B) was characterized by a scanning electron microscope (SEM), revealing significant reconstruction from a smooth surface to a roughened porous flower-like network. For GDEs, we formed electrodes containing Cu on porous expanded polytetrafluoroethylene (ePTFE) substrates via physical vapor deposition (PVD) (Figure 2C), denoted as either GDE-275 or GDE-1000 depending on the deposited Cu thickness in nm. NF formation was translated to a GDE by employing the same procedure used on electrodes (referred to as GDE-275-NF and GDE-1000-NF), as exposure time and solution composition can modulate the electrode nanostructure and surface area.[33] Both top (Figure 2D) and cross-section (Figure 2F) SEM images of these electrodes further show that the dense Cu layer formed by PVD (Figure 2E) results in a nanoflower structure, similar in feature and pore size (~100-200 nm) as foil-NF (Figure 2B and S3). Additionally, we validated the stability of this structure by conducting SEM after electrochemical testing, which showed some sintering while the major morphological features are maintained (Figure S4). The X-ray photoelectron spectroscopy (XPS) spectra of the Cu 2p region for the NF electrodes exhibited a broad peak at ~933.5 eV and satellite features in the range of 940-945 eV, both corresponding to the Cu^{2+} oxidation state (Figure S5). Similarly, the corresponding X-ray diffraction (XRD) patterns reveal the presence of CuO in agreement with Cu^{2+} observed via XPS (Figure S6).

To estimate the ECSA of each electrode, we performed cyclic voltammetry to measure the double-layer capacitance in a non-Faradaic potential window (Figure S7). The RF, defined as the ratio of ECSA to geometric area of the electrode, resulted in values of 2 and 185 for foil-pc and foil-NF, respectively (Figure 2G). This substantial increase of 92x in ECSA is likely due to large amounts of Cu available within the foil-pc electrode that converted to NF. In comparison, GDE-275 and GDE-1000 resulted in comparable RFs of 11 and 13 before NF formation, respectively, despite their difference in the catalyst-layer thickness; as bulk Cu atoms are shielded from the electrolyte, they do not affect the ECSA measurements nor participate in CO_2R. After NF

formation the average RFs scaled with the PVD Cu thickness, with values of 33 (GDE-275-NF) and 185 (GDE-1000-NF). We found that nanostructuring an initial PVD layer of 1000 nm thickness (GDE-1000) led to a near identical roughness as that of the foil-NF. It is noted that while the wet etching process increases the ECSA, it does so by simultaneously altering both catalyst thickness and porosity (Figure 2E-F). The resulting increase in the ECSA for GDEs (3x and 14x as rough) is notably less relative to the foil electrodes due to higher ECSA of non-nanostructured GDE-275 and GDE-1000 samples (Table S7).

2.2. Understanding potential-dependent selectivity trends

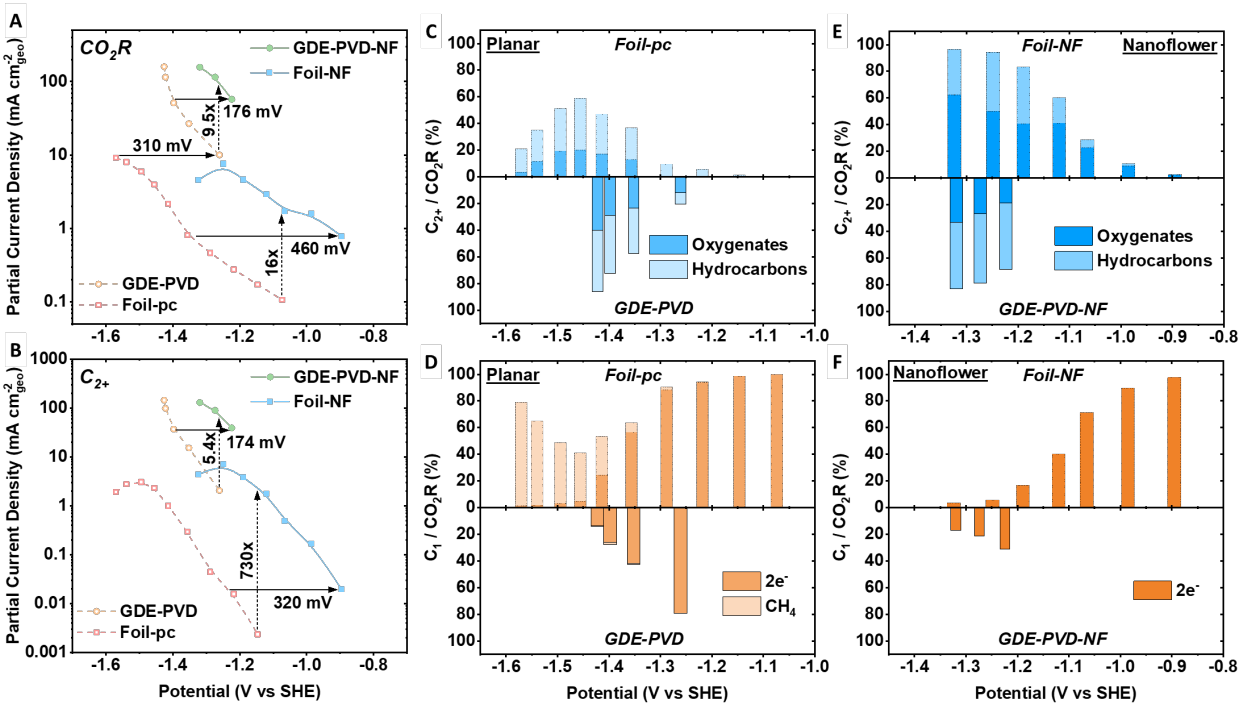

Figure 3. Potential shifts and fractional selectivity towards C_{2+} and C_1 products from CO_2 reduction

(A and B) CO_2R (A) and C_{2+} (B) partial current densities for foil electrodes (foil-pc and foil-NF) and GDEs (GDE-1000 and GDE-1000-NF) at various operating potentials.

(C-F) Fraction of C_{2+} products (C) and C_1 products (D) for foil and GDEs with planar morphology. Fraction of C_{2+} products (E) and C_1 products (F) for foil and GDEs with nanoflower morphology. C_{2+} products divided into multi-carbon oxygenate (C_{2+} OXY) and multi-carbon hydrocarbon (C_{2+} HC). C_1 products divided into two electron single carbon ($2e^-$ C_1) and CH_4. Foil-pc data adapted from previous work.[27]

To understand the changes in the electrocatalytic activity and selectivity with changing electrode structure, we tested CO_2R performance under both liquid- and vapor-fed conditions using the same corresponding electrochemical reactor and underlying substrate. These comparisons are done by plotting the applied potential with respect to the standard hydrogen electrode (V_{SHE}), which allows for the assessment of trends based on an absolute potential reference and thus circumventing variable pH corrections and differences in electrolyte concentration. It is important to note that the GDEs can operate at much greater geometric

current densities (J_{geo}) for CO_2R than the foils due to substantially increased diffusivity and smaller diffusion lengths of CO_2 in vapor- and aqueous phase, respectively.[39] Thus, any improvements in applied potential or J_{geo} will be conservative compared to those on the RHE scale (denoted as V_{RHE}), as the GDEs will result in a higher shift due to increased pH from higher J_{geo}. When comparing electrodes of the same architecture, we use V_{RHE} where appropriate (see SI). Additionally, the results shown at each current density were repeated three times to establish statistical significance, which exhibited reasonable standard deviations of the data (Table S1-S6).

Between the foils and GDEs, we observe a >310 mV potential difference between foil-pc and GDE-PVD at a CO_2R J_{geo} of 10 mA cm^{-2}, highlighting the impact of increased CO_2 mass transport and higher ECSA within the GDEs.[39,40] Within the same electrode architecture, there is a positive shift in the operating potential window with the higher RF (NF morphology) electrodes (Figure 3A and B), alluding to the activation overpotential dependence on RF. At a CO_2R J_{geo} of ~0.8 mA cm^{-2}, the foil electrodes resulted in a maximum potential shift of 460 mV. The GDEs resulted in a smaller shift of 176 mV, as the RF ratio is smaller than that of the foil. For the thinner GDE-275, there was an even smaller shift of 62 mV at the same CO_2R J_{geo} of 57 mA cm^{-2} (Figure S10). At a constant potential, the CO_2R J_{geo} increases by up to 16x with the foil-NF electrodes, whereas up to 9.5x is achieved with the GDEs. In terms of C_{2+} J_{geo}, the shift in the potential range for the foil electrodes is reduced to 320 mV, whereas the GDEs have largely maintained the potential shift of 174 mV. Thus, the degree of overpotential shift can vary depending on the electrode type and operating potential window. We infer that the greater difference (460 – 320 mV) between the foil electrodes is due to CO, $HCOO^-$, and CH_3COO^- being formed at lower overpotentials due to an increased ECSA (Figure S11). Overall, this indicates that the increased catalyst surface area helps to decrease the overpotentials in the predominantly activation-controlled regime, and thus increase energy efficiency, while maintaining the rate at which CO_2R products are generated for both GDEs and foil electrodes.

The foil-NF electrode is highly selective towards two-electron single-carbon ($2e^-$ C_1) products starting at −0.49 V_{RHE} (-0.89 V_{SHE}) (Figure S8). Peak selectivity towards CO (72.2%) and $HCOO^-$ (31.8%) are observed along with a modest 8.5% FE toward H_2; formation of these $2e^-$ products is due to the low overpotential similar to other reported high RF systems operating in

similar to more positive potentials.[18,22,22,41–43] With increasing overpotentials (<–0.58 V_{RHE} or -0.98 V_{SHE}), higher selectivity towards C_{2+} products including C_2H_4, C_2H_5OH, C_3H_7OH, CH_3COO^-, and small quantities of C_2H_6 are measured. Furthermore, an oxygenate-to-hydrocarbon ratio of up to 11.8 is measured on the foil-NF at lower overpotentials (Figure S17). Previously, we observed this enhanced C_{2+} oxygenate formation for CO_2R and CO reduction correlating with increased ECSA and low overpotentials.[18,33] Additionally, the combination and increased quantity of oxide-derived active sites present in foil-NF may promote selectivity towards oxygenates.[26,44,45] For GDE samples, C_2H_4 formation on the NF samples exceeds that of both PVD samples at 71 mA cm^{-2}, with lower selectivity towards C_2H_5OH and H_2 (Figure S9). Effects due to internal diffusion within the pores such as trapping[46] and local pH changes may aid in the formation of further-reduced products at low J_{geo}.[33,47] Our modeling analysis shows that sufficient CO_2 concentration (>21 mM) and less alkaline pH are expected throughout the rougher, more porous catalyst layers, supporting the aforementioned effects (Figures S38-39). However, the effects of decreasing pH and CO_2 concentration are more pronounced at the higher current densities of 143 and 214 mA cm^{-2}, resulting in the NF samples exhibiting lower selectivity towards C_{2+} products compared to the thinner PVD catalyst layers.

To better understand the distribution of CO_2R products, the fractional selectivity for both the foil and GDE is given in Figure 3C-F. The GDE-PVD demonstrates significantly greater C_{2+}/CO_2R ratio compared to that of the foil-pc electrode at similar applied potentials (Figure 3C). Remarkably, C_{2+} oxygenates are observed at potentials as positive as –1.26 V_{SHE} with the GDE, whereas only C_{2+} hydrocarbons are found in the case of the foil. This earlier onset corresponds to higher oxygenate-to-hydrocarbon ratios on the GDE-PVD than the foil (Figures S17-18). Additionally, the GDE shows a lower preference for C_1 formation compared to the foil (Figure 3D). We posit this is due to enhanced C-C coupling with higher average CO_2 concentration throughout GDEs (Figures S35 and S38) and a local pH effect caused by increased current density.[29] Comparing foil electrodes, CH_4 is not observed on the foil-NF due to the overpotential shift being in the positive direction while activation-controlled. For the foil-pc, CH_4 increases at potentials <–1.28 V_{SHE}, becoming the majority CO_2R product due to limited solubility of CO_2.[37] Despite these

differences, exclusive formation towards $2e^-$ products for both foil and GDE is observed at potentials >−1.28 V_{SHE}, which is again attributed to the low overpotential.

Unlike the planar Cu morphology, greater C_{2+}/CO_2R fractions are obtained with the foil-NF electrode under liquid-fed aqueous conditions compared to those of the GDE-1000-NF in a similar potential window (−1.20 to −1.32 V_{SHE}) (Figure 3E). Relative to the foil, we see greater fractions towards $2e^-$ product formation at higher overpotentials on the GDE due to *CO desorption when higher concentrations of CO_2 are present (Figure 3F).[48] However, this is opposite for the NF morphology, which results in a higher oxygenate-to-hydrocarbon ratio for the foil compared to the GDE (Figures S17-18). Because both electrodes exhibit similar morphology, porosity (Figures 2F and S2), and RF (~185), we deduce that the increased oxygenate fraction on the foil-NF is likely influenced by differences in the microenvironment.[12] The concentration and residence times of adsorbates can vary between electrode architectures at lower current densities. For example, the GDE architecture may result in more effective removal of hydroxide than the foil setup due to flowing electrolyte and CO_2 being fed on the GDL side, which reduces local oxygen concentration and the propensity for oxygenate production. We observe a clear preference towards C_{2+} production for all NF electrodes at potentials >−0.95 V_{RHE} (Figures S14-S16), with up to 10x enhancement in C_{2+}/CO_2R for the foil NF at ~−0.9 V_{RHE} (-1.3 V_{SHE}). Thus, the influence from the combination of both electrode RF and microenvironment lead to the observed enhancements in C_{2+} formation, not just the potential. Furthermore, the increase of the C_{2+}/CO_2R ratios associated with the GDE-NF samples are not observed at potentials <−0.95 V_{RHE} (<-1.41 V_{SHE}) (Figures S14-16). The effects of ECSA on the current density-potential behavior and product selectivity are more prominent in liquid-fed systems as compared to vapor-fed systems at potentials more positive than −0.95 V_{RHE}, which may suggest decreasing influence from local reaction environments in GDEs.

2.3. Activity comparison of liquid- and vapor-fed systems

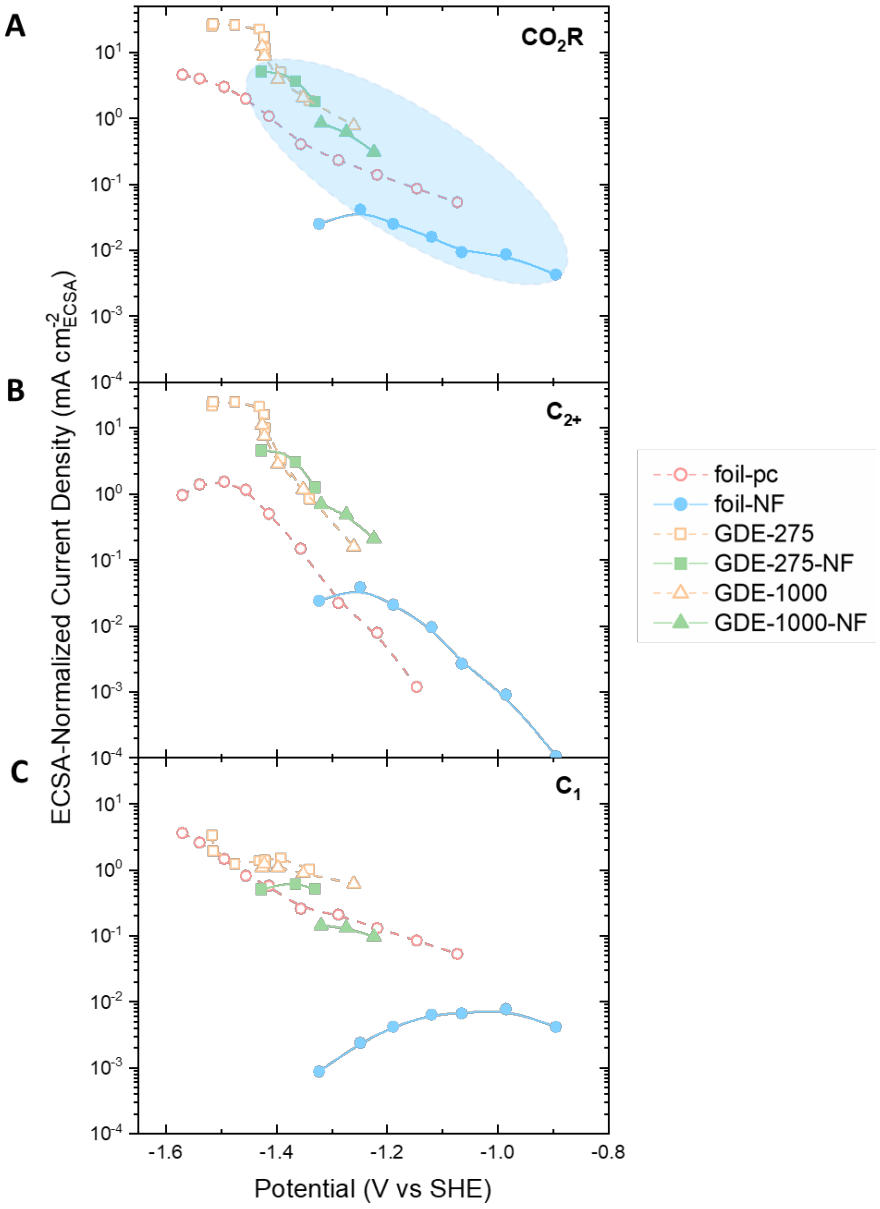

Figure 4. Comparison of foil and gas-diffusion electrode samples.
(A-C) ECSA-normalized partial current density towards (A) CO_2R products, (B) C_{2+} products, and (C) C_1 products as a function of potential (V vs SHE) for foil and GDE samples. Blue oval in (A) indicates J-V slopes towards CO_2R appear similar while activation-controlled.

Due to the importance of the local microenvironment and conditions on CO_2R selectivity, we examine the data in terms of the local current density (i.e., ECSA-normalized) or average turnover frequency per active site for each electrode.[49] There is an increase in the ECSA-normalized current density (J_{ECSA}) towards CO_2R for the GDEs compared to foil electrodes (Figure 4A).[40] We identify the slopes for CO_2R activity to be similar for all the samples in this study prior to mixed-control (shaded blue). Furthermore, the J_{ECSA} towards CO_2R for all GDE samples collapse onto a single curve, validating the observed potential shift associated with J_{geo} under activation-control. Thus, we observe little to no enhancement in the intrinsic activity of Cu towards CO_2R with increasing ECSA in the form of a GDE, similar to what is observed in liquid-fed systems using foil electrodes.[9,13]

To assess changes in product activity, we provide results for the individual products (Figures S19-S26), and C_{2+} (Figure 4B) and C_1 (Figure 4C) product groupings. The current-voltage (J-V) slopes for C_2H_4, C_2H_5OH, and C_3H_7OH appear consistent across all samples while in the activation-controlled regime, suggesting the rate-limiting step plausibly remains unaffected (Figure S22-S24).[50] The changing slope for CH_3COO^- compared to other C_{2+} products (Figure S25) reinforces the hypotheses regarding ECSA and pH effects resulting in divergent reaction mechanisms for these products.[51,52] However, the activities towards C_{2+} products show light promotion ascribed to the NF GDEs. While the foil-NF sample appears to suppress both CO_2R and HER (Figure S26) when compared to foil-pc, it promotes C_{2+} product formation by an order of magnitude (~10x at –1.15 V vs SHE). The average number of electrons per molecule reaffirms that the formation of C_{2+} products is achieved with the rougher NF samples at lower overpotentials (Figure S28). We infer the contribution on C_{2+} product activity from changing ECSA and morphology may be larger for liquid-fed CO_2R on foil electrodes than vapor-fed CO_2R on GDEs. Additionally, the discernable asymptotic and/or decreasing J_{ECSA} indicates the samples may be entering a mixed-control regime at varying potentials.

The enhancements in C_{2+} products suggest a corresponding suppression of C_1 product formation with all NF electrodes (Figure 4C). The NF samples show poor activity towards $HCOO^-$ compared to the planar counterparts (Figure S20). The suppression of this terminal reaction pathway leads to the formation of *CO, the common intermediate for all other CO_2R products.[9]

316 The overall product distribution supports the preference for *CO dimerization, as CO formation
317 is also suppressed on the NFs like $HCOO^-$ (Figure S19). Additionally, little to no formation of CH_4
318 on the NFs leads to a combined lower J_{ECSA} towards C_1 products (Figure S20). Interestingly, the
319 GDE-1000-NF has a lower fraction of products going through the COR pathway compared to foil-
320 NF (Figure S29); we posit the effects of concentration overpotential and lower residence times
321 of adsorbed intermediates on the NF GDEs may allow for more facile *CO desorption.
322 Additionally, this may be related to the quantity of hydrogen evolving; the activity towards
323 hydrogen results in similar J-V slopes for all NF electrodes, whereas asymptotic regions are
324 present on the foil-pc and PVD electrodes where CO_2R is dominant (Figure S26). Based on this
325 analysis, we provide insight onto the varying contributions of microenvironment and morphology
326 on product activity and selectivity.

2.4. Investigating RF influence on overpotential shift via analytical and modeling approaches

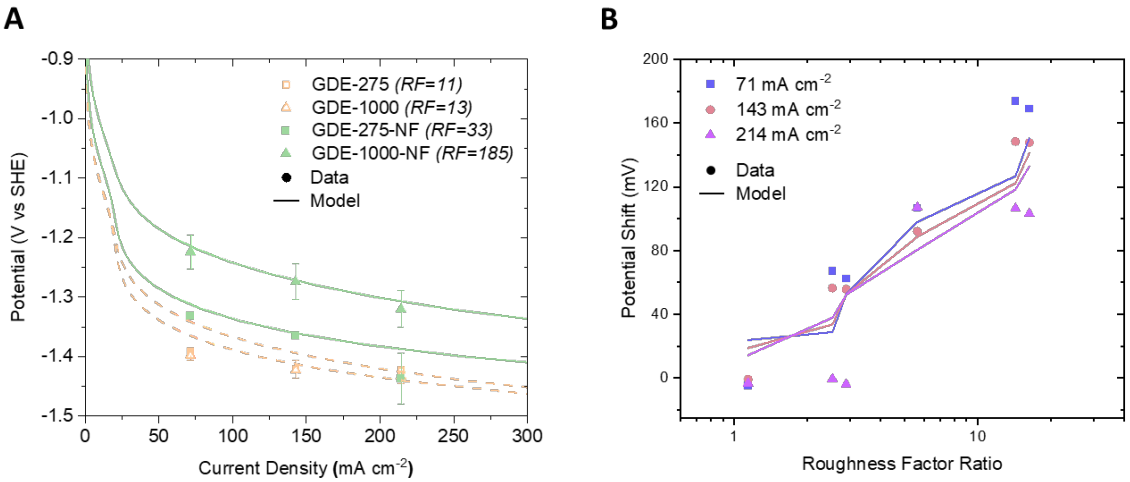

Figure 5. Relationship between roughness factor ratio and overpotential shift derived from experimental results and predicted by 1D steady-state model.
(A) Potential (V vs. SHE) resulting from various applied current densities obtained with the four GDEs from experiment (scatter), and the predicted relationship from the model using an average of $6e^-$ per CO_2 (solid and dashed lines).
(B) Potential shift resulting from six possible combinations of RF ratios from the four GDE samples (scatter) and the model prediction using the Tafel parameters extracted from Figure 5A (line).

To probe further the relationship between RF and overpotential shift, we simulate the effects using a 1D, steady-state GDE catalyst-layer model for CO_2R and HER reactions (complete description in Section S3). We account for CO_2R and HER by using single electrochemical reactions with the average electrons passed per product; two electrons for HER and 5-6 electrons per CO_2 molecule reduced. This is based on the observation that the majority species are two-carbon products within the potential range that was tested as shown in the experimental data (Figure S28)):

$$CO_2 + H_2O + 6e^- \rightarrow \text{products} + 6\,OH^-, \quad U^0 = 0.02\,V \text{ vs } RHE$$

$$2H_2O + 2e^- \rightarrow H_2 + 2OH^-, \quad U^0 = 0.00\,V \text{ vs } RHE$$

This reaction kinetics are modeled using the Tafel expressions,

$$j_{CO_2R} = j_{\mathrm{CO_2R,0}}\left(\frac{c_{\mathrm{CO_2}}}{c_{\mathrm{CO_2}}^{\mathrm{ref}}}\right)\exp\left(\frac{\alpha_{\mathrm{CO_2}R}F}{RT}\left(\phi_s - \phi_l - \left(U^0_{\mathrm{CO_2R}} - \frac{2.303RT}{F}\mathrm{pH}\right)\right)\right) \quad (1)$$

$$j_{\mathrm{HER}} = j_{\mathrm{HER,0}}\exp\left(\frac{\alpha_{\mathrm{HER}}F}{RT}\left(\phi_s - \phi_l - \left(U^0_{\mathrm{HER}} - \frac{2.303RT}{F}\mathrm{pH}\right)\right)\right). \quad (2)$$

The Tafel parameters ($\alpha_{\mathrm{CO_2R}}$, α_{HER}, $j_{\mathrm{CO_2R,0}}$ and $j_{\mathrm{HER,0}}$) are determined using a pH-corrected foil electrode model (complete description in Section S3.1). Piecewise-linear and linear fits accurately describe the foil data from the foil-pc and foil-NF samples, respectively (Figure S35). The electrochemical reaction rate for species i is calculated as

$$R_i = \sum_h \frac{a_v \nu_{i,h} j_h}{n_h F} \quad (3)$$

where $\nu_{i,h}$ is the stoichiometric coefficient for species i in electrochemical reaction h, n_h is the number of electrons in electrochemical reaction h. The specific surface area is calculated using the dimensions and measured ECSA of each catalyst layer, which is normalized by the roughness factor of the foil electrode data that was used to fit the kinetics,

$$a_v = \frac{RF_{\mathrm{GDE}}}{RF_{\mathrm{foil}}} \cdot \frac{1}{L_{CL}} \cdot S \quad (4)$$

where S is the saturation. The saturation accounts for the fraction of the catalyst layer surface that is not wetted by the electrolyte and a value of 0.64 is assumed for an ideally-wetted catalyst layer.[53] Dividing the RF of the GDE by the RF of the foil-NF electrode normalizes the exchange current densities to the ECSA at which the kinetic parameters were extracted. By incorporating CO_2 and ion-transport effects, electrode parameters, and bulk electrolyte reactions (as described by Weng et al.),[53] we predict the J-V relationships for the four GDEs labeled by their RFs (Figure 5A). The results show that the Tafel fit to the foil-NF data, when scaled by ECSA, give an accurate prediction of the J-V relationships for all GDE samples. Additionally, there was little sensitivity to the average number of electrons between five and six (Figure S41). This suggests that our utilization of ECSA in the modified Tafel description is a valid method for estimating the trend of decreasing overpotential with increasing RF for the GDEs.

We then determined six RF ratios (dividing any two electrode RFs) from combinations of the four GDE samples (Figure S31A). Further comparison of the modeling results provided a semi-

logarithmic relationship between the ratio of RFs and the difference in applied potentials at 71 and 143 mA cm^{-2} (Figure 5B). The computational model predicts similar shifts in potential for the various RF ratios, further corroborating the use of the number of electrons per CO_2 molecule as an effective approach towards understanding activity relationships between HER and CO_2R. Furthermore, these results suggest some proportional dependence of overpotential shift on the ratio of RFs (Figure S31), despite the complex reaction networks on the catalytic surface. These differences are exacerbated at a J_{geo} of 214 mA cm^{-2}, where a notable deviation from linearity is observed along with increased deviations between sample potentials (Figure S32). The surface CO_2 concentration from the model indicates a drastic decrease with thicker electrodes and a commensurate increase in the local pH at high current densities (Figures S38-39). Additionally, we posit observations including increased overpotential (due to low CO_2 concentration) and hydrogen evolution are indicative of entering a mixed-control regime.

The resulting slopes of 151 mV dec^{-1} (at 71 mA cm^{-2}) and 128 mV dec^{-1} (at 143 mA cm^{-2}) vary due to the differences in catalyst-layer thickness, morphology, and product selectivity within each combination of electrodes. Additionally, the contributions from surface faceting cannot be ignored and are also tied to the applied potential.[28] We extend this analysis by measuring the current-potential slopes from the J_{ECSA} of the total and CO_2R reactions showing 123 and 116 mV dec^{-1}, respectively (Figure S30). This is in agreement with the slopes of potential shift vs RF ratio, which are in fact both *b* according to the definition of the Tafel expression (full the derivation in the SI). Specifically, the slopes obtained using potential shifts at a total J_{geo} of 143 mA cm^{-2} from both the experiment (128 mV dec^{-1}), and the model (123 mV dec^{-1}) are comparable. This is likely due to the majority of total current being comprised of CO_2R current, thereby the slope derived from J_{CO2R} results in a similar value of 116 mV dec^{-1}. We observe that the above trends in potential shift and RF ratio apply across all electrodes in this work, regardless of electrode architecture (Figure S33). At any near-equivalent value of J_{geo} for total and CO_2R reactions, the range of potential shifts increases with RF. These results signify RF/ECSA as an important descriptor for developing computational models that deepen our understanding of current-potential relationships. A more robust model including microkinetic parameters for various intermediates and mechanisms can further elucidate the dependence on RF.

3. Conclusion

In this work, we identify and bridge knowledge gaps between liquid- and vapor-fed CO_2 reduction systems, using active surface area as a descriptor to understand the effects of changing local environments and resultant activity and selectivity trends. For the liquid-fed CO_2R system, the Cu foil-NF electrode demonstrates up to 735x increase in geometric current density towards CO_2R (−0.75 V vs RHE) and an overpotential shift up to 460 mV compared to the foil-planar. A preference towards multi-carbon products (>95% of CO_2R is C_{2+}) is observed as compared to the foil-pc from previous work. Within vapor-fed devices, rougher GDEs provide similar overpotential shifts (~170 mV) and geometric current-density enhancements (~10x towards CO_2R). Such overpotential shifts can lead to increased energy efficiency while maintaining a desired current density, however, selectivity trends do not necessarily extend between electrode architectures. Additionally, the NF morphology prefers multi-carbon product formation on an activity basis, even though the J-V slopes from the ECSA-normalized current densities from different electrodes are similar. With a 1D computational model using a simplified Tafel-description, the observed potential shifts are strongly suggested to be related to the RF ratios of electrodes when activation-controlled. Through this comparative investigation, we demonstrate a general strategy that utilizes electrode engineering efforts to translate foil electrodes from liquid-fed to GDEs for more industrially relevant operating conditions. Our approach towards understanding the interplay of current-potential relationships, electrode formulation, and local reaction environment can be applied to a variety of systems and reactions for improved design and performance.

4. Methods

4.1. Electrode Preparation and Characterization

A cleaned and polished copper foil was immersed in an aqueous solution containing 0.25 M sodium hydroxide and 62.5 mM ammonium persulfate at 60 ℃ for one hour to form cupric oxide nanoflowers (See SI for full preparation procedure). The same procedure was used to make the nanostructured GDE samples from a layer of copper deposited via e-beam physical vapor deposition on the expanded polytetrafluoroethylene (ePTFE) gas-diffusion-layer (GDL) substrate. The as-prepared electrodes were characterized by scanning electron microscopy (SEM) to confirm nanoflower morphology, and focused ion-beam (FIB) SEM was used to measure electrode thicknesses. X-ray photoelectron spectroscopy (XPS) and X-ray diffraction (XRD) were used to confirm the oxidation and crystal structure of the copper catalyst, respectively. The electrodes were electrochemically pre-reduced prior to performing CO_2 reduction at a potential of -0.75 V vs Ag|AgCl, the electrochemically active surface area (ECSA) was determined by performing double-layer capacitance measurements via cyclic voltammetry (CV).

4.2. Electrochemical Evaluation

For the liquid-fed system, a CO_2-saturated 0.1 M $KHCO_3$ electrolyte was fed with humidified CO_2 at the flow rate of 20 sccm. For the vapor-fed system, CO_2 gas at 10 sccm is directly introduced to the backside of the GDE in addition to the CO_2-saturated 1 M $KHCO_3$ electrolyte at the front of the GDE. For the liquid-fed system, chronoamperometry was used for 1 hour, while chronopotentiometry was used for vapor-fed analyses. IR-compensation was performed by an average of measured resistances (taken every three minutes) over the electrolysis period. The entire protocol was repeated three times to confirm reproducibility for each condition.

4.3. Reactor and System Set Up

A custom polycarbonate electrochemical cell and advanced manufactured electrochemical cell was used for liquid-fed and vapor-fed CO_2R experiments, respectively.[33,38]

Both cells formed a three-electrode system: (1) foil and gas diffusion electrodes were used as working electrodes and exposed to the electrolyte; (2) a platinum foil (Alfa Aesar; 99.99% trace metals basis) and IrO_2 (Dioxide Materials) were used as counter electrodes for liquid-fed and vapor-fed systems, respectively; (3) an Ag/AgCl electrode was used as the reference electrode through a Luggin capillary. Anion-exchange membranes comprised of (Selemion AMV, AGC Inc.) and Fumasep were used in between the working and counter electrode compartments for liquid- and vapor-fed systems, respectively.

4.4. Product Analysis

Product identification and quantification were conducted according to protocols described in detail in our previous work.[29,37,38] For each tested operating condition, 1 mL of reactor exhaust gas was injected multiple times into a GC (SRI Instruments; Multiple Gas #3, 8610C) during the electrolysis period to analyze the concentration of products in the gas phase. After CA/CP measurements, the electrolyte was collected, and then the liquid-phase products were analyzed by using water suppression ^{1}H NMR (600 MHz, Varian Inova and 500 MHz, Avance III HD Bruker with Prodigy cryoprobe). The anolyte was also analyzed in the same way to account for acetate and formate species that crossed over the membrane due to their anionic character.

5. References

1. Obama, B. (2017). The irreversible momentum of clean energy. Science *355*, 126–129.

2. Chu, S., Cui, Y., and Liu, N. (2017). The path towards sustainable energy. Nature materials *16*, 16.

3. Davis, S.J., Lewis, N.S., Shaner, M., Aggarwal, S., Arent, D., Azevedo, I.L., Benson, S.M., Bradley, T., Brouwer, J., Chiang, Y.-M., et al. (2018). Net-zero emissions energy systems. Science *360*, eaas9793.

4. Majumdar, A., and Deutch, J. (2018). Research Opportunities for CO2 Utilization and Negative Emissions at the Gigatonne Scale. Joule *2*, 805–809.

5. Pacala, S., and Socolow, R. (2004). Stabilization Wedges: Solving the Climate Problem for the Next 50 Years with Current Technologies. Science *305*, 968–972.

6. Welch, A.J., Dunn, E., DuChene, J.S., and Atwater, H.A. (2020). Bicarbonate or Carbonate Processes for Coupling Carbon Dioxide Capture and Electrochemical Conversion. ACS Energy Lett. *5*, 940–945.

7. Bushuyev, O.S., De Luna, P., Dinh, C.T., Tao, L., Saur, G., van de Lagemaat, J., Kelley, S.O., and Sargent, E.H. (2018). What should we make with CO2 and how can we make it? Joule *2*, 825–832.

8. Kuhl, K.P., Hatsukade, T., Cave, E.R., Abram, D.N., Kibsgaard, J., and Jaramillo, T.F. (2014). Electrocatalytic conversion of carbon dioxide to methane and methanol on transition metal surfaces. Journal of the American Chemical Society *136*, 14107–14113.

9. Nitopi, S., Bertheussen, E., Scott, S.B., Liu, X., Engstfeld, A.K., Horch, S., Seger, B., Stephens, I.E., Chan, K., Hahn, C., et al. (2019). Progress and Perspectives of Electrochemical CO2 Reduction on Copper in Aqueous Electrolyte. Chemical reviews.

10. Xie, H., Wang, T., Liang, J., Li, Q., and Sun, S. (2018). Cu-based nanocatalysts for electrochemical reduction of CO2. Nano Today *21*, 41–54.

11. Raciti, D., and Wang, C. (2018). Recent advances in CO2 reduction electrocatalysis on copper. ACS Energy Letters *3*, 1545–1556.

12. Hahn, C., and Jaramillo, T.F. (2020). Using Microenvironments to Control Reactivity in CO2 Electrocatalysis. Joule *4*, 292–294.

13. Resasco, J., and Bell, A.T. (2020). Electrocatalytic CO2 Reduction to Fuels: Progress and Opportunities. Trends in Chemistry *2*, 825–836.

14. Kas, R., Yang, K., Bohra, D., Kortlever, R., Burdyny, T., and Smith, W.A. (2020). Electrochemical CO2 reduction on nanostructured metal electrodes: fact or defect? Chem. Sci. *11*, 1738–1749.

15. Pang, Y., Burdyny, T., Dinh, C.-T., Kibria, M.G., Fan, J.Z., Liu, M., Sargent, E.H., and Sinton, D. (2017). Joint tuning of nanostructured Cu-oxide morphology and local electrolyte programs high-rate CO2 reduction to C2H4. Green Chem. *19*, 4023–4030.

16. Wu, M., Zhu, C., Wang, K., Li, G., Dong, X., Song, Y., Xue, J., Chen, W., Wei, W., and Sun, Y. (2020). Promotion of CO2 Electrochemical Reduction via Cu Nanodendrites. ACS Appl. Mater. Interfaces *12*, 11562–11569.

17. Clark, E.L., Resasco, J., Landers, A., Lin, J., Chung, L.-T., Walton, A., Hahn, C., Jaramillo, T.F., and Bell, A.T. (2018). Standards and protocols for data acquisition and reporting for studies of the electrochemical reduction of carbon dioxide. ACS Catalysis *8*, 6560–6570.

18. Hahn, C., Hatsukade, T., Kim, Y.-G., Vailionis, A., Baricuatro, J.H., Higgins, D.C., Nitopi, S.A., Soriaga, M.P., and Jaramillo, T.F. (2017). Engineering Cu surfaces for the electrocatalytic conversion of CO2: Controlling selectivity toward oxygenates and hydrocarbons. Proceedings of the National Academy of Sciences *114*, 5918–5923.

19. Feng, X., Jiang, K., Fan, S., and Kanan, M.W. (2016). A direct grain-boundary-activity correlation for CO electroreduction on Cu nanoparticles. ACS central science *2*, 169–174.

20. Feng, X., Jiang, K., Fan, S., and Kanan, M.W. (2015). Grain-Boundary-Dependent CO2 Electroreduction Activity. J. Am. Chem. Soc. *137*, 4606–4609.

21. Garza, A.J., Bell, A.T., and Head-Gordon, M. (2018). Mechanism of CO2 reduction at copper surfaces: pathways to C2 products. ACS Catalysis *8*, 1490–1499.

22. Jiang, K., Huang, Y., Zeng, G., Toma, F.M., Goddard, W.A., and Bell, A.T. (2020). Effects of Surface Roughness on the Electrochemical Reduction of CO2 over Cu. ACS Energy Letters.

23. Calle-Vallejo, F., Loffreda, D., Koper, M.T.M., and Sautet, P. (2015). Introducing structural sensitivity into adsorption–energy scaling relations by means of coordination numbers. Nature Chem *7*, 403–410.

24. Yang, P.-P., Zhang, X.-L., Gao, F.-Y., Zheng, Y.-R., Niu, Z.-Z., Yu, X., Liu, R., Wu, Z.-Z., Qin, S., Chi, L.-P., et al. (2020). Protecting Copper Oxidation State via Intermediate Confinement for Selective CO_2 Electroreduction to C_{2+} Fuels. J. Am. Chem. Soc. *142*, 6400–6408.

25. Zhuang, T.-T., Pang, Y., Liang, Z.-Q., Wang, Z., Li, Y., Tan, C.-S., Li, J., Dinh, C.T., De Luna, P., Hsieh, P.-L., et al. (2018). Copper nanocavities confine intermediates for efficient electrosynthesis of C3 alcohol fuels from carbon monoxide. Nature Catalysis, 1.

26. Eilert, A., Cavalca, F., Roberts, F.S., Osterwalder, J., Liu, C., Favaro, M., Crumlin, E.J., Ogasawara, H., Friebel, D., Pettersson, L.G.M., et al. (2017). Subsurface Oxygen in Oxide-Derived Copper Electrocatalysts for Carbon Dioxide Reduction. J. Phys. Chem. Lett. *8*, 285–290.

27. Ren, D., Fong, J., and Yeo, B.S. (2018). The effects of currents and potentials on the selectivities of copper toward carbon dioxide electroreduction. Nature communications *9*, 925.

28. De Luna, P., Quintero-Bermudez, R., Dinh, C.-T., Ross, M.B., Bushuyev, O.S., Todorović, P., Regier, T., Kelley, S.O., Yang, P., and Sargent, E.H. (2018). Catalyst electro-redeposition controls morphology and oxidation state for selective carbon dioxide reduction. Nature Catalysis *1*, 103.

29. Wang, L., Nitopi, S.A., Bertheussen, E., Orazov, M., Morales-Guio, C.G., Liu, X., Higgins, D.C., Chan, K., Nørskov, J.K., Hahn, C., et al. (2018). Electrochemical Carbon Monoxide Reduction on Polycrystalline Copper: Effects of Potential, Pressure, and pH on Selectivity toward Multicarbon and Oxygenated Products. ACS Catal. *8*, 7445–7454.

30. Durst, J., Siebel, A., Simon, C., Hasché, F., Herranz, J., and A. Gasteiger, H. (2014). New insights into the electrochemical hydrogen oxidation and evolution reaction mechanism. Energy & Environmental Science *7*, 2255–2260.

31. Dinh, C.-T., Burdyny, T., Kibria, M.G., Seifitokaldani, A., Gabardo, C.M., de Arquer, F.P.G., Kiani, A., Edwards, J.P., De Luna, P., Bushuyev, O.S., et al. (2018). CO2 electroreduction to ethylene via hydroxide-mediated copper catalysis at an abrupt interface. Science *360*, 783–787.

32. Liu, X., Schlexer, P., Xiao, J., Ji, Y., Wang, L., Sandberg, R.B., Tang, M., Brown, K.S., Peng, H., Ringe, S., et al. (2019). pH effects on the electrochemical reduction of CO (2) towards C 2 products on stepped copper. Nature communications *10*, 32.

33. Wang, L., Nitopi, S., Wong, A.B., Snider, J.L., Nielander, A.C., Morales-Guio, C.G., Orazov, M., Higgins, D.C., Hahn, C., and Jaramillo, T.F. (2019). Electrochemically converting carbon monoxide to liquid fuels by directing selectivity with electrode surface area. Nature Catalysis *2*, 702–708.

34. de Arquer, F.P.G., Dinh, C.-T., Ozden, A., Wicks, J., McCallum, C., Kirmani, A.R., Nam, D.-H., Gabardo, C., Seifitokaldani, A., Wang, X., et al. (2020). CO2 electrolysis to multicarbon products at activities greater than 1 A cm- 2. Science *367*, 661–666.

35. Ma, W., Xie, S., Liu, T., Fan, Q., Ye, J., Sun, F., Jiang, Z., Zhang, Q., Cheng, J., and Wang, Y. (2020). Electrocatalytic reduction of CO2 to ethylene and ethanol through hydrogen-assisted C–C coupling over fluorine-modified copper. Nat Catal *3*, 478–487.

36. Wang, Y., Wang, Z., Dinh, C.-T., Li, J., Ozden, A., Kibria, M.G., Seifitokaldani, A., Tan, C.-S., Gabardo, C.M., Luo, M., et al. (2020). Catalyst synthesis under CO 2 electroreduction favours faceting and promotes renewable fuels electrosynthesis. Nature Catalysis *3*, 98–106.

37. Kuhl, K.P., Cave, E.R., Abram, D.N., and Jaramillo, T.F. (2012). New insights into the electrochemical reduction of carbon dioxide on metallic copper surfaces. Energy & Environmental Science *5*, 7050–7059.

38. Corral, D., Feaster, J.T., Sobhani, S., DeOtte, J.R., Lee, D.U., Wong, A.A., Hamilton, J., Beck, V.A., Sarkar, A., Hahn, C., et al. (2021). Advanced manufacturing for electrosynthesis of fuels and chemicals from CO2. Energy Environ. Sci. *5*, 3064–3074.

39. Weekes, D.M., Salvatore, D.A., Reyes, A., Huang, A., and Berlinguette, C.P. (2018). Electrolytic CO2 reduction in a flow cell. Accounts of chemical research *51*, 910–918.

40. Higgins, D.C., Hahn, C., Xiang, C., Jaramillo, T.F., and Weber, A.Z. (2018). Gas-Diffusion Electrodes for Carbon-Dioxide Reduction: A New Paradigm. ACS Energy Letters.

41. Raciti, D., Livi, K.J., and Wang, C. (2015). Highly dense Cu nanowires for low-overpotential CO2 reduction. Nano letters *15*, 6829–6835.

42. Min, S., Yang, X., Lu, A.-Y., Tseng, C.-C., Hedhili, M.N., Li, L.-J., and Huang, K.-W. (2016). Low overpotential and high current CO2 reduction with surface reconstructed Cu foam electrodes. Nano Energy *27*, 121–129.

43. Ma, M., Djanashvili, K., and Smith, W.A. (2015). Selective electrochemical reduction of CO 2 to CO on CuO-derived Cu nanowires. Physical Chemistry Chemical Physics *17*, 20861–20867.

44. Lum, Y., and Ager, J.W. (2019). Evidence for product-specific active sites on oxide-derived Cu catalysts for electrochemical CO 2 reduction. Nature Catalysis *2*, 86–93.

45. Mistry, H., Varela, A.S., Kühl, S., Strasser, P., and Cuenya, B.R. (2016). Nanostructured electrocatalysts with tunable activity and selectivity. Nature Reviews Materials *1*, 1–14.

46. Dutta, A., Rahaman, M., Mohos, M., Zanetti, A., and Broekmann, P. (2017). Electrochemical CO2 Conversion Using Skeleton (Sponge) Type of Cu Catalysts. ACS Catal. *7*, 5431–5437.

47. Klingan, K., Kottakkat, T., Jovanov, Z.P., Jiang, S., Pasquini, C., Scholten, F., Kubella, P., Bergmann, A., Roldan Cuenya, B., Roth, C., et al. (2018). Reactivity Determinants in Electrodeposited Cu Foams for Electrochemical CO2 Reduction. ChemSusChem *11*, 3449–3459.

48. Tan, Y.C., Lee, K.B., Song, H., and Oh, J. (2020). Modulating Local CO2 Concentration as a General Strategy for Enhancing C- C Coupling in CO2 Electroreduction. Joule *4*, 1104–1120.

595 49. Benck, J.D., Hellstern, T.R., Kibsgaard, J., Chakthranont, P., and Jaramillo, T.F. (2014).
596 Catalyzing the Hydrogen Evolution Reaction (HER) with Molybdenum Sulfide
597 Nanomaterials. ACS Catal. *4*, 3957–3971.

598 50. Peng, H., Tang, M.T., Liu, X., Schlexer Lamoureux, P., Bajdich, M., and Abild-Pedersen, F.
599 (2021). The role of atomic carbon in directing electrochemical CO $_{(2)}$ reduction to
600 multicarbon products. Energy Environ. Sci., 10.1039.D0EE02826F.

601 51. Luc, W., Fu, X., Shi, J., Lv, J.-J., Jouny, M., Ko, B.H., Xu, Y., Tu, Q., Hu, X., Wu, J., et al. (2019).
602 Two-dimensional copper nanosheets for electrochemical reduction of carbon monoxide to
603 acetate. Nature Catalysis *2*, 423–430.

604 52. Garza, A.J., Bell, A.T., and Head-Gordon, M. (2018). Mechanism of CO2 Reduction at Copper
605 Surfaces: Pathways to C2 Products. ACS Catal. *8*, 1490–1499.

606 53. Weng, L.-C., Bell, A.T., and Weber, A.Z. (2018). Modeling gas-diffusion electrodes for CO 2
607 reduction. Physical Chemistry Chemical Physics *20*, 16973–16984.

608
609

6. Acknowledgements

This work was performed at both the Department of Chemical Engineering at Stanford University and Lawrence Livermore National Laboratory, funded by a cooperative research and development agreement with TOTAL American Services, Inc. (affiliate of TOTAL SE) under agreement number TC2307. This work was performed under the auspices of the U.S. Department of Energy by Lawrence Livermore National Laboratory under Contract DE-AC52-07NA27344 and was supported by Laboratory Directed Research and Development funding under project 19-SI-005. Project conceptualization and liquid-fed CO_2 reduction experiments was performed by Daniel Corral, Stephanie Nitopi, and Lei Wang with the Joint Center for Artificial Photosynthesis, a DOE Energy Innovation Hub, supported through the Office of Science of the U.S. Department of Energy under Award Number DE-SC0004993. Alex King was supported by a NSF Graduate Fellowship (DGE 1752814) and along with Adam Weber acknowledge support from the Liquid Sunlight Alliance, which is supported by the U.S. Department of Energy, Office of Science, Office of Basic Energy Sciences, Fuels from Sunlight Hub under Award Number DE-SC0021266. Daniel Corral thanks the Stanford Graduate Fellowship, as well as the GEM Fellowship at Stanford University and Lawrence Livermore National Laboratory. The authors thank and appreciate guidance and discussions from colleagues including Julie Hamilton, Dr. Alan Landers, David Koshy, Kabir Abiose, Dr. McKenzie Hubert, Kyra Yap, Prof. Carlos Morales-Guio, Prof. Andrew Wong, Prof. Drew Higgins, Dr. Shaffiq Jaffer, and Dr. Amitava Sarkar. The authors thank Alex King and Dr. Adam Weber for modeling guidance and helpful discussions. The authors thank the Nuclear Magnetic Resonance Spectroscopy Facilities, and part of this work was performed at the Stanford Nano Shared Facilities (SNSF), supported by the National Science Foundation under award ECCS-2026822. The authors thank Maryann C. Tung for collecting SEM images using FIB. The authors thank the Nuclear Magnetic Resonance Spectroscopy and Cleanroom Facilities at Lawrence Livermore National Laboratory.

7. Author contributions

D.C. and D.L. contributed significantly and equally to this work. Writing – original draft: D.C., D.L., V.M.E., S.N., and J.E.A.; Writing – Review & Editing: D.C., D.L., V.M.E., S.N., J.E.A., L.W., A.J.K., J.T.F., Y.L., A.Z.W., S.E.B., E.B.D., V.A.B., C.H., and T.F.J.; Conceptualization: D.C., D.L., S.N., and L.W.; Investigation: D.C., D.L., V.M.E., S.N., J.E.A., L.W., and A.J.K.; Methodology: D.C., D.L., V.M.E., J.E.A., A.J.K., and V.A.B.; Formal Analysis: D.C., J.E.A., V.M.E., A.J.K., A.Z.W., and V.A.B.; Software: V.M.E., A.J.K., A.Z.W., and V.A.B.; Validation: D.C., D.L., S.N., V.M.E., J.E.A., L.W., J.T.F., Y.L., and V.A.B.; Project Administration: D.C., D.L., S.E.B., E.B.D., V.A.B., C.H., and T.F.J.; Funding Acquisition: D.C., A.J.K., A.Z.W., S.E.B., E.B.D., V.A.B., C.H., and T.F.J.

8. Author Information

Daniel Corral	0000-0003-0778-4832
Dong Un Lee	0000-0001-7591-5350
Victoria M. Ehlinger	0000-0001-7333-1271
Stephanie Nitopi	0000-0001-6815-0628
Jaime E. Avilés Acosta	0000-0002-2259-1935
Lei Wang	0000-0002-1931-7767
Alex J. King	0000-0002-3156-1607
Jeremy T. Feaster	0000-0003-0729-9650
Yi-Rung Lin	0000-0003-0331-3822
Adam Z. Weber	0000-0002-7749-1624
Sarah E. Baker	0000-0003-4695-3918
Eric B. Duoss	0000-0002-5473-2528
Victor A. Beck	0000-0002-0625-9545
Christopher Hahn	0000-0002-2772-6341
Thomas F. Jaramillo	0000-0001-9900-0622